Supporting Information: Large Polaron Formation and its Effect on Electron Transport in Hybrid Perovskite

Fan Zheng and Lin-wang Wang*

Joint Center for Artificial Photosynthesis and Materials Sciences Division, Lawrence Berkeley National Laboratory, Berkeley, California 94720, USA.

E-mail: lwwang@lbl.gov

An outline of the methods used in this work

A direct DFT would be almost impossible to study $MAPbI_3$ with large polaron (more than 1 million atoms), therefore, we choose TB to describe the electronic structure fitted based on small system DFT results. Here we outline the different techniques used to study different phenomena.

Large polaron formation: Following Eq.1, the polaron lattice polarization potential is reflected in the screened potential energy (E^{P}) which also depends on charge density. By minimizing the total energy in terms of wavefunction (as shown in Eq.2), the large polaron ground state wavefunction can be obtained in the self-consistent way so that the potential energy benefit over wins the kinetic energy penalty, and a localized states could be formed.

Large polaron dynamics: As we have shown in Ref. 1, the random molecular rotation (i.e. dynamic disorder) can localize the charge and drive the carrier motion. By including the large polaron effect, we want to understand 1) how the large polaron affects the dynamic disorder driving carrier transport; 2) how the PbI_3^- sublattice vibration at finite temperature

influences the charge carrier in addition to the large polaron.

There is no single direct *ab initio* calculation to handle such a large system, including its dynamics. We have developed different well-fitted and tested model Hamiltonians to capture different physics.

For MA molecular rotation, we have developed a layer-dependent screened dipole-dipole interaction model to simulate the dynamics of the molecular re-orientation. For a given molecular orientation of a large system, the potential generated by these dipoles to Pb and I atoms can be computed. Such potential is used in the TB model to determine the wave function localization.

The above dipole model provides the effect of the MA rotation (which is described by a kinetic Monte Carlo) to the lattice potential on Pb and I. There are two effects for the PbI_3^- sublattice movement, which is also the main topic of our study in the current paper. The first is its movement for polarization in response to the Coulomb potential caused by the localized electron (which forms the large polaron). This is described by the polarization model (Eq.1 and Eq.2). The second is the effects caused by the thermal random lattice vibration.

The effects of PbI_3^- lattice vibration on the TB Hamiltonian, particularly the Pb–I bond length change, is described by a classical MD simulation of the $MAPbI_3$ lattice. This classical MD is based on a force field potential.[2] The result of this MD can provide the bond length changes of neighboring Pb–I with respect to time, which in term is used to modify their coupling constant changes in the TB model. Our TB model has been well-tested to be able to reproduce the DFT band structure with distorted Pb-I bonds as presented in Fig. S1b.

However, besides the TB coupling constant changes due to the PbI_3 vibration, such lattice vibration also causes a small Pb and I onsite energy fluctuation. Unfortunately, it is difficult to describe this onside potential fluctuation using the classical MD results. Our small-system DFT *ab initio* MD shows that the evolution of this onsite-energies of Pb and I are relatively simple. Such dynamics can be fitted with a simple Langevin dynamics. Therefore, we have

fit a Langevin model to reproduce the *ab initio* onsite-energy dynamics. Then this model is applied to the 48×48×48 system to get the dynamics of all the Pb and I onsite-energies.

All the above effects, for the on-site energies, as well as coupling constants are simulated in dynamic ways (Kinetic Monte Carlo for MA rotation, classical MD for PbI_3^- sublattice for TB coupling constant, and Langevin dynamics for Pb and I onsite energy due to PbI_3^- vibrations). They are added to the $H(t)$ to carry out the nonadiabatic MD based on Eq.5. During solving Eq.5, we have included the important screening effects due to the PbI_3^- lattice (i.e. the large polaron effects to the localized electron wave function), and a delay response (Eq.6) is used to take care of the finite response time of the large polaron formation and annihilation.

Tight-binding model

To reduce the computational cost, we implement the tight-binding (TB) model to compute the electronic structures of $MAPbI_3$. The parameters of the TB are based on the previous work in Ref. 3. In this model, we consider 13 atomic orbitals for one unit cell, which includes one Pb atom with s, p_x, p_y, p_z and three I atoms with p_x, p_y, p_z for each. The orbitals of the molecules at A-site are not included, since these orbitals do not hybridize with the edge states. Instead, their effect is mainly applied to the structural distortion and the potential. Here, only nearest-neighbor hopping is considered, which gives good agreement with the DFT-calculated band structures for the band edge states as shown in Fig.S1a. Fig.S1a is for a highly symmetric structure with all the Pb and I atoms in their high-symmetric positions (12 atom cubic cell). Here, the DFT obtained band gap is manually shifted to be consistent with experiment (~1.7 eV) to fit the TB model. The deviations at the top of the conduction band is mainly because of the molecular orbitals existed in the DFT calculation. Including next-nearest-neighbor hopping, particularly between the neighboring I–I atoms will improve the valence bands below the band edge. Since we are interested only in the conduction band minimum state, including such next-nearest-interaction will greatly increase the computational cost but does not improve the band edge state fitting signifi-

cantly. Our TB parameters are also consistent with the Hamiltonian obtained by maximally localized Wannierization using Wannier90.[4] The hopping strength for the equilibrium structure are set as -1.01 eV, -0.53 eV and 1.83 eV, for *s*-*p* σ, *p*-*p* π, *p*-*p* σ, respectively. Here, the DFT band structure is computed based on a 12 atom $MAPbI_3$ unit cell, with 50 Ryd energy cutoff using GGA exchange-correlation functional. A 8×8× k-point grid is used for the self-consistent calculation followed by a band structure non-self-consistent calculation. Spin-orbit coupling (SOC) is added in the pseudopotential and DFT.

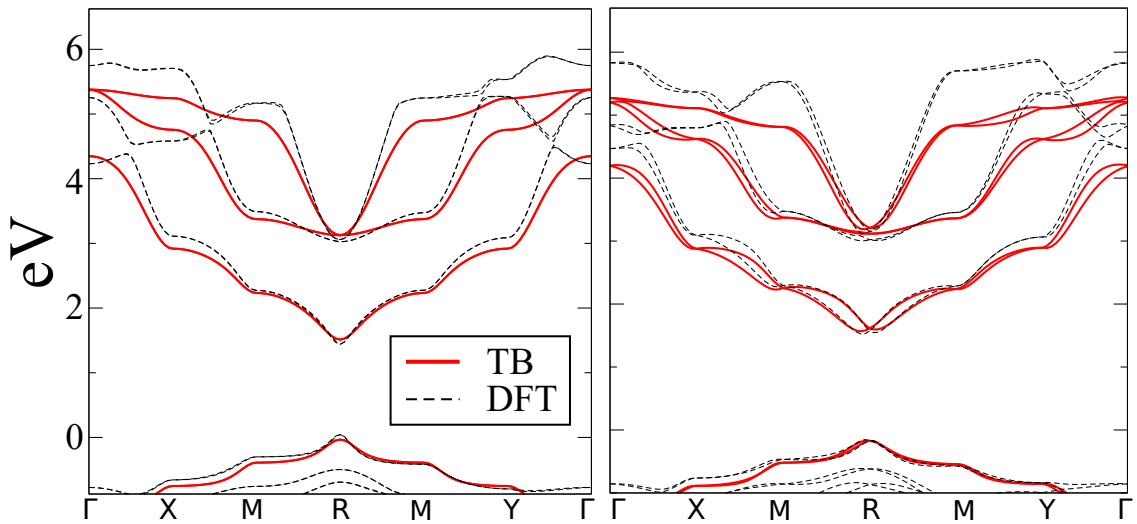

Figure 1: The comparison between the fitted TB model and the DFT calculated band structure for equilibrium structure (left) and distorted structure (right). 0 eV indicates the position of VBM. Here, the band gap is shifted (including DFT) to 1.7 eV to be consistent with the experimental band gap.

Owing to the significance of SOC in OMHPs, we also implement SOC in our TB, where the wavefunction is described by a spinor with two spin components. Therefore, the basis set to build up the Hamiltonian is doubled. We consider onsite SOC for Pb and I atoms, and their coupling strength is obtained via fitting as well as Wannierization procedure.[3,5] The SOC onsite coupling is set as 0.54 eV and 0.34 eV for Pb and I, respectively.

Our TB model also captures the structural distortion to the electronic structure. This is realized by varying the hopping strength with respect to change of bond length as $h = h_0 e^{-\lambda(b-b_0)}$ (see main text, equilibrium bond length $b_0 = 3.157$Å). The λ obtained from

Ref. 6 is fitted from the Wannierization of structures from a MD trajectories with different distortions. They are chosen as $\lambda = 1.4\text{Å}^{-1}$ for *s*-*p* σ and $\lambda = 1.0\text{Å}^{-1}$ for *p*-*p* π bonds, respectively. For *p*-*p* σ, a linear fitting tends to fit better. TB solved band structure under distorted structure can well reproduce DFT band structure as shown in Fig.S1b, including the large Rashba splitting for the bottom of conduction band.

If we use 48×48×48 supercell in our calculation, the Hamiltonian matrix size will be 2,875,392×2,875,392. Direct diagonalization is impossible either for computational effort or memory requirement. Since the TB Hamiltonian is generally a sparse matrix, we implement the sparse-matrix iterative eigen solver ARPACK based on the MPI parallelization (P_ARPACK).[7] In our calculation, only a few eigenstates near the band edges are needed, which greatly reduces the cost of the calculations.

Calculating phonon and dielectric constant

DFT calculation with SOC is performed to obtain the phonons using plane-wave packages PWmat and Quantum Espresso[8–10] with generalized gradient approximation (GGA)[11] and norm-conserving pseudopotential (SG15).[12] A converged energy cutoff as 50 Ryd and 6×6×4 k-point grid is used for the self-consistent calculation for the tetragonal phase. By applying density-functional perturbation to the fully relaxed tetragonal structure of $MAPbI_3$ with 48 atoms ($\sqrt{2} \times \sqrt{2} \times 2$), the high frequency dielectric constant is calculated as 4.5, consistent to the single-particle approximation calculation.[13] Phonons under harmonic approximation at the zone center is obtained with their frequencies and eigen-modes. By computing the Born effective charge, the low frequency dielectric constant is computed as 16.5 by summing over contributions from all the modes as following:

$$
\begin{aligned}
Z^*_{\mu\alpha} &= \sum_{i\beta} \frac{z^*_{i\alpha\beta} a_{\mu,i\beta}}{\sqrt{m_i}} \\
\epsilon_{\mu\alpha\beta} &= \frac{Z^*_{\mu\alpha} Z^*_{\mu\beta}}{4\pi^2 \epsilon_0 V \nu_\mu^2}
\end{aligned}
\tag{1}
$$

where μ is the phonon mode, $z_{i\alpha\beta}$ is the Born effective charge for atom i along α and β directions (along x, y and z), ν_μ and $a_{\mu,i\beta}$ are the phonon frequency and phonon mode, respectively, V is the volume of the unit cell and m_i is the mass of atom i. The total low frequency dielectric constant originating from the atomic vibrations and electronic screening will be $\epsilon_0 = \frac{1}{3}\sum_{\mu\alpha}\epsilon_{\mu\alpha\alpha} + \epsilon_\infty = 21$.

Using this way, we can also compute the dielectric constant from each phonon mode. Shown in Fig.S2 is the phonon-mode resolved dielectric constants (ϵ_μ) averaged for xx, yy and zz. We find that the low energy phonons (ten modes below 1.3 THz out of 144 modes in total) yields dielectric constant more than 10, contributing more than half of the total dielectric constant from phonons, which showing their significant role in forming large polaron.

LO phonons provide the effective screening to form large polaron, which also contribute the major part of the static dielectric constant. In this material, the LO phonon frequency can be as low as below 0.9 THz. In order to obtain a more definitive ω_{LO} (used for Eq.3), we average the phonon frequencies based on their dielectric constant as shown in Fig.S2. The averaged LO frequency weighed by dielectric constant of each phonon is estimated to be around 2.39 THz. Its corresponding α is around 3.24.

The Born-effective charges of all the ions are also used to estimated spatial displacement in order to generate the polarization potential shown in Fig. 1b. For simplicity, we average the Born-effective charges for their diagonal elements, and we obtain 4.4 for Pb, -1.8 for I and 1.0 for MA molecule. Following $Z^*_{i,\alpha\beta} = V\frac{\Delta P_\alpha}{\Delta R_{i,\beta}}$ (Z^* is the Born-effective charge, V is the volume, ΔP and ΔR are the change of polarization and spatial displacements in the specified volume, respectively), ΔP can be computed by calculating derivative of polarization potential. We estimate the order of the spatial displacements for all the ions is in average around 0.001 Å, which is smaller than the thermal fluctuations around 0.01Å~0.1 Å.

DFT calculation of supercell to fit dipole-dipole model

In order to fit the layer-dependent dielectric constants used for the dipole-dipole inter-

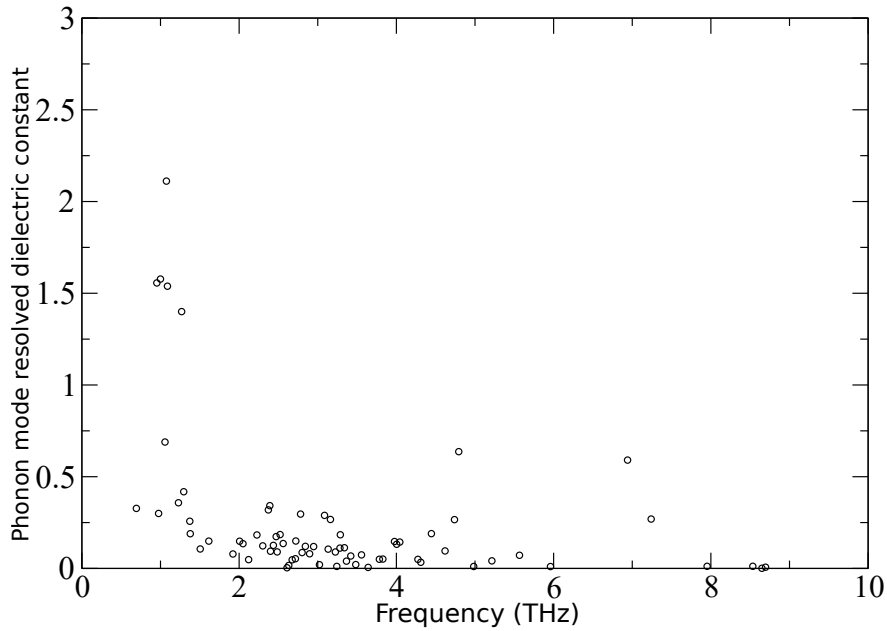

Figure 2: Phonon-mode resolved dielectric constant ϵ_μ averaged for xx, yy and zz. Here, only phonon modes lower than 10 THz are shown. Phonons with higher modes are mainly intra-molecular vibrations.

action model (see main text), we perform DFT calculation of a relatively small supercell 3×3×3. We generate three supercells with different molecular orientations as the initial structures. Full relaxations with all the forces below 0.01 eV/Å are performed for the three structures. The potential for each atom can be extracted from our DFT calculation with PWmat. Here, the potential for a molecule is the averaged potentials of the eight atoms of this molecule. In our layer-dependent dipole-dipole model, a radius of 150 Å is converged when evaluating the total energy for each dipole so that the energy difference is under 1 meV.

ab initio molecular dynamics (MD)

With the same setup discussed above, we perform *ab initio* MD for a 3×3×3 supercell. Based on the relation of rotation rate γ and temperature discussed in Ref. 14 as $\gamma = A\mathrm{e}^{-\frac{E_\mathrm{a}}{K_\mathrm{B}T}}$ with E_a set as 10 meV, the MD simulations are performed under different temperatures corresponding to the different rotation rates (0.27 ps^{-1} (320K), 0.25 ps^{-1} (263K), 0.2 ps^{-1} (174K), 0.167 ps^{-1} (137K), 0.125 ps^{-1} (102K) and 0.1 ps^{-1} (85K)). The time step for the

MD is set as 2 fs. The onsite potential of Pb and I atoms are collected from the MD trajectory. Then their onsite-potential correlation functions are computed and averaged for each temperature. The magnitude of the model potential is also checked for each temperature to make sure they are consistent with DFT results. During the MD, all the A-site molecules are fixed, so the potential change of Pb and I are purely from the PbI_3^- sublattice phonons.

Langevin model dynamics

The Fourier analysis of the onsite potential extracted from *ab initio* MD trajectories reveals that the onsite energy of Pb and I are mostly controlled by two phonon modes (0.002 fs^{-1} and 0.0036 fs^{-1}). Thus, the dynamics of Pb (or I) will be the combination of the two oscillators $x(0.002\text{fs}^{-1})$ and $x(0.0036\text{fs}^{-1})$ as $x_1 = c_1^1 x(0.002\text{fs}^{-1}) + c_2^1 x(0.0036\text{fs}^{-1})$ and $x_2 = c_1^2 x(0.002\text{fs}^{-1}) + c_2^2 x(0.0036\text{fs}^{-1})$. For both oscillators, the damping constant is chosen as 0.0019 fs^{-1} for Pb and 0.00105 fs^{-1} for I (from fitting). The magnitude of the random force is chosen so that the magnitude of the onsite variation is consistent to the *ab initio* MD at different temperatures. In addition to the onsite autocorrelation function, we also fit to the neighboring Pb–I pair correlation function. To achieve the neighboring Pb–I coupling, we further mix the trajectories of x_1 and x_2 as $V_{\text{Pb}} = \alpha_1^{\text{Pb}} x_1 + \beta_1^{\text{Pb}} \sum_{\text{neigh}} x_2$ and $V_{\text{I}} = \alpha_2^{\text{I}} x_2 + \beta_2^{\text{I}} \sum_{\text{neigh}} x_1$. Then, we fit all the parameters including the mixing weights to the DFT, so that the averaged auto- and neighboring pair correlation functions match the *ab initio* MD results.

Dynamic disorder potential fluctuation by MA

By randomly choosing four line along [001] direction in the supercell, the dynamic disorder induced onsite potential of the Pb atoms along these four lines can be plotted in Fig.S3. These potentials are chosen from the Hamiltonians which are solved to give the wavefunction shown in Fig.1c (dynamic disorder only) and Fig.1d (including dynamic disorder and large polaron effect). As shown in this graph, the lowest potential is around -0.2 V.

Classical MD simulation

The classical MD is performed with LAMMPs.[15] The force field is based on the work in

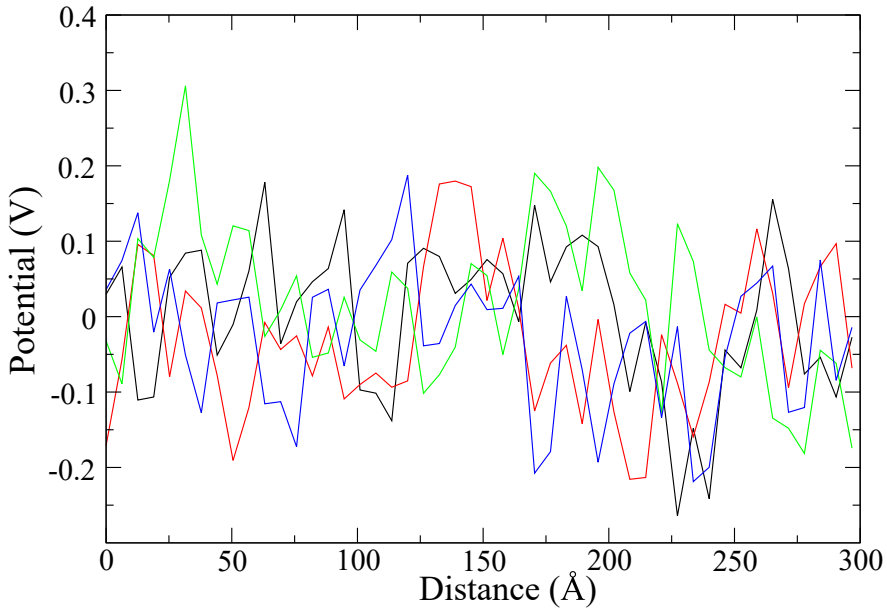

Figure 3: The extracted Pb onsite potential along four lines chosen randomly along [001] direction. These potentials are generated by the random orientation of the molecular dipoles in the supercell. These potentials are added to the Hamiltonian H_0 to solve the wavefunction shown in Fig.1c (dynamic disorder only) and Fig.1d (including dynamic disorder and large polaron effect).

Ref. 2, where the organic molecules are described with AMBER force field, inorganic PbI_3^- sublattice is described with Buckingham potential, and the inorganic–organic interaction is described as sum of the Buckingham, electrostatic, and Lennard-Jones terms. In our simulation, a time step of 0.5 fs is used. The NVT ensemble with fixed cell is used in order to maintain the cubic structure, which greatly simplifies our wavefunction evolution. We start from relatively low temperature and increase it slowly to the temperature we required. The system is fully equilibrated before its trajectory is used for wavefunction evolution. The 20 wavefunction evolutions use uncorrelated MD trajectories.

Carrier transport

Different τ of polaron formation and annihilation. As illustrated in Eq. 6, τ controls the polaron formation and annihilation time, and this retarding effect is included in our large polaron dynamic simulations. Such time should always be finite owing to the relatively slow phonon motion as well as phonon-phonon scatterings. Taking 6ps molecular rotation as an

example, shown in Fig. S4 is the $R^2(t)$ computed with time for τ~0 fs, $\tau = 80$ fs, $\tau = 150$ fs, and $\tau = 300$ fs. By increasing the polaron formation/annihilation time τ, the diffusion constant is reduced slightly (τ~0 fs is special). However, such change in terms of τ is quite small compared to other effects such as different molecular rotation rate, or PbI_3^- sublattice vibration effect. Therefore, we use $\tau = 80$ fs in our simulations.

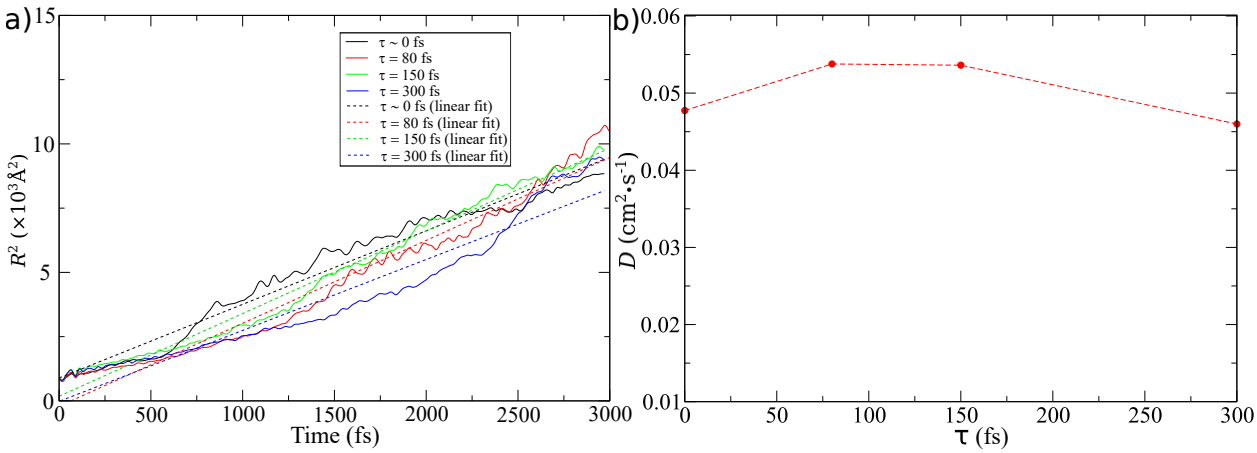

Figure 4: a) $R^2(t)$ with respect to time computed at different τ. Here, we take 6ps molecular rotation rate as an example. b) The obtained diffusion constants under different τ.

Mobility. Fig.S 5 shows the comparison of the minimum of polarization potentials for the cases with and without PbI_3^- sublattice phonon effect. In order to deplete the effect of dynamic disorder, these two cases are performed with exact same molecular dipole rotation for each MC step. Although phonons including onsite energy and hopping strength variation tend to bring more driving force of the carrier motion, such additional randomness localizes the carrier more and yields deeper polarization potential, which may slow down the carrier dynamics in the opposite.

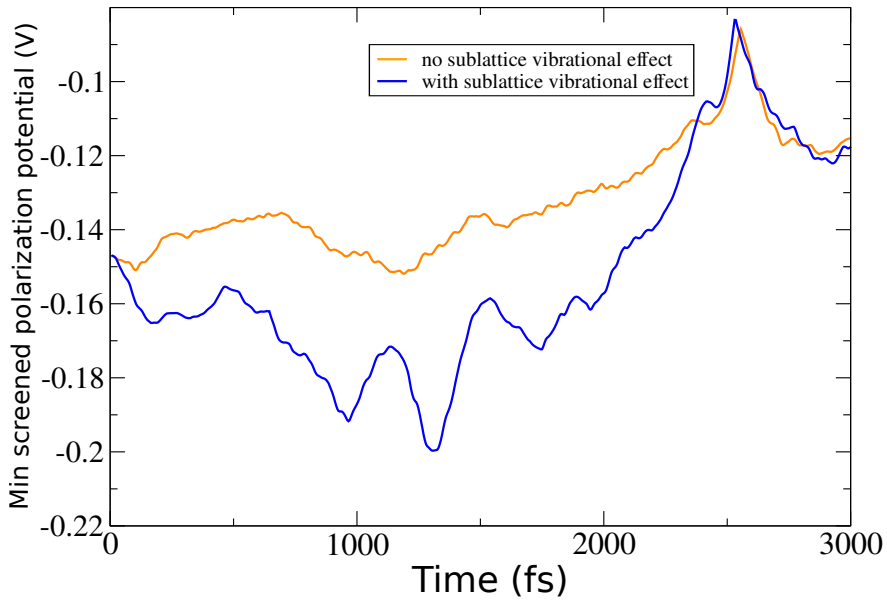

Figure 5: The extracted minimum of the polarization potential with and without PbI_3^- sublattice phonon effect. For these two simulations, in order to deplete the effect of dynamic disorder, exact same MA molecular rotations are used for each MC step.

References

(1) Ma, J.; Wang, L.-W. Nanoscale Charge Localization Induced by Random Orientations of Organic Molecules in Hybrid Perovskite CH $_3$ NH $_3$ PbI $_3$. *Nano Letters* **2015**, *15*, 248–253.

(2) Mattoni, A.; Filippetti, A.; Saba, M. I.; Delugas, P. Methylammonium Rotational Dynamics in Lead Halide Perovskite by Classical Molecular Dynamics: The Role of Temperature. *The Journal of Physical Chemistry C* **2015**, *119*, 17421–17428.

(3) Zheng, F.; Tan, L. Z.; Liu, S.; Rappe, A. M. Rashba Spin–Orbit Coupling Enhanced Carrier Lifetime in CH3NH3PbI3. *Nano Letters* **2015**, *15*, 7794–7800.

(4) Marzari, N.; Mostofi, A. A.; Yates, J. R.; Souza, I.; Vanderbilt, D. Maximally Localized Wannier Functions: Theory and Applications. *Reviews of Modern Physics* **2012**, *84*, 1419–1475.

(5) Kim, M.; Im, J.; Freeman, A. J.; Ihm, J.; Jin, H. Switchable S = 1/2 and J = 1/2

Rashba Bands in Ferroelectric Halide Perovskites. *Proceedings of the National Academy of Sciences* **2014**, *111*, 6900–6904.

(6) Mayers, M. Z.; Tan, L. Z.; Egger, D. A.; Rappe, A. M.; Reichman, D. R. How Lattice and Charge Fluctuations Control Carrier Dynamics in Halide Perovskites. *Nano Letters* **2018**, *18*, 8041–8046.

(7) Maschho, K. J.; Sorensen, D. C. P ARPACK: An E Cient Portable Large Scale Eigenvalue Package for Distributed Memory Parallel Architectures. *Applied Parallel Computing in Industrial Problems and Optimization, Lecture Notes in Computer Science* **1996**, *1184*.

(8) Jia, W.; Fu, J.; Cao, Z.; Wang, L.; Chi, X.; Gao, W.; Wang, L.-W. Fast Plane Wave Density Functional Theory Molecular Dynamics Calculations on Multi-GPU Machines. *Journal of Computational Physics* **2013**, *251*, 102–115.

(9) Jia, W.; Cao, Z.; Wang, L.; Fu, J.; Chi, X.; Gao, W.; Wang, L.-W. The Analysis of a Plane Wave Pseudopotential Density Functional Theory Code on a GPU Machine. *Computer Physics Communications* **2013**, *184*, 9–18.

(10) Giannozzi, P. et al. QUANTUM ESPRESSO: A Modular and Open-Source Software Project for Quantum Simulations of Materials. *Journal of Physics: Condensed Matter* **2009**, *21*, 395502.

(11) Perdew, J. P.; Burke, K.; Ernzerhof, M. Generalized Gradient Approximation Made Simple. *Physical review letters* **1996**, *77*, 3865.

(12) Hamann, D. R. Optimized Norm-Conserving Vanderbilt Pseudopotentials. *Physical Review B* **2013**, *88*, 085117.

(13) Zheng, F.; Brehm, J. A.; Young, S. M.; Kim, Y.; Rappe, A. M. Substantial Optical

Dielectric Enhancement by Volume Compression in LiAsSe 2. *Physical Review B* **2016**, *93*.

(14) Ma, J.; Wang, L.-W. The Nature of Electron Mobility in Hybrid Perovskite $CH_3NH_3PbI_3$. *Nano Letters* **2017**, *17*, 3646–3654.

(15) Plimpton, S. Fast parallel algorithms for short-range molecular dynamics. *Journal of computational physics* **1995**, *117*, 1–19.